Combined molecular dynamics–direct simulation Monte Carlo computational study of laser ablation plume evolution

Michael I. Zeifman[a] and Barbara J. Garrison[b]
Department of Chemistry, 152 Davey Laboratory, Pennsylvania State University, University Park, Pennsylvania 16802

Leonid V. Zhigilei[c]
Department of Material Science and Engineering, 116 Engineer's Way, University of Virginia, Charlottesville, Virginia 22904

(Received 11 March 2002; accepted for publication 24 May 2002)

A two-stage computational model of evolution of a plume generated by laser ablation of an organic solid is proposed and developed. The first stage of the laser ablation, which involves laser coupling to the target and ejection of molecules and clusters, is described by the molecular dynamics (MD) method. The second stage of a long-term expansion of the ejected plume is modeled by the direct simulation Monte Carlo (DSMC) method. The presence of clusters, which comprise a major part of the overall plume at laser fluences above the ablation threshold, presents the main computational challenge in the development of the combined model. An extremely low proportion of large-sized clusters hinders both the statistical estimation of their characteristics from the results of the MD model and the following representation of each cluster size as a separate species, as required in the conventional DSMC. A number of analytical models are proposed and verified for the statistical distributions of translational and internal energies of monomers and clusters as well as for the distribution of the cluster sizes, required for the information transfer from the MD to the DSMC parts of the model. The developed model is applied to simulate the expansion of the ablation plume ejected in the stress-confinement irradiation regime. The presence of the directly ejected clusters drastically changes the evolution of the plume as compared to the desorption regime. A one-dimensional self-similar flow in the direction normal to the ablated surface is developed within the entire plume at the MD stage. A self-similar two-dimensional flow of monomers forms in the major part of the plume by about 40 ns, while its counterpart for large clusters forms much later, leading to the plume sharpening effect. The expansion of the entire plume becomes self-similar by about 500 ns, when interparticle interactions vanish. The velocity distribution of particles cannot be characterized by a single translational temperature; rather, it is characterized by a spatially and direction dependent statistical scatter about the flow velocity. The cluster size dependence of the internal temperature is mainly defined by the size dependence of the unimolecular dissociation energy of a cluster. [DOI: 10.1063/1.1494129]

I. INTRODUCTION

Laser ablation of organic solids is a complex physical phenomenon, which involves a wide range of diverse processes, from molecular excitation to generation of pressure wave in the target and a collective expulsion of molecules and clusters into an ambient background. A clear understanding of the physics defining the plume expansion is of fundamental importance in such applications of laser ablation as thin films deposition and mass spectrometry. Quality of the deposited films in pulsed laser deposition[1,2] and quality of mass spectra in matrix assisted laser desorption ionization[3,4] are critically dependent on the velocity distributions of the ejected species and their spatial distributions in the plume.

The laser ablation community had long adopted a thermal desorption model in which laser irradiation results in a layer-by-layer evaporation of molecules from the target surface. The following expansion of the vapor cloud has been treated either by means of analytical models,[5,6] numerically,[7,8] or in simulation.[9–11] Several experimental effects were explained, including strong forward peaking of the angular distribution in the plume[6] and spatial segregation of light and heavy particles in the case of a binary target.[12] The presence of submicro-[13] and even micron-sized[14] particles in the plume cannot be explained, however, in the framework of the thermal desorption model.[15] Moreover, the actual speed of the expansion front is a factor of 2–3 faster than that predicted for typical vaporization temperatures.[8]

Molecular dynamics (MD) simulations of laser ablation in organic solids[16] performed with the breathing sphere model[17] have provided some insights into the physical mechanisms responsible for material disintegration and ejection in laser ablation. In particular, the MD simulations have identified two distinct irradiation regimes. In the *desorption* regime, realized at low laser fluences, the abovementioned thermal desorption model is a reasonable approximation. In

[a]Electronic mail: miz3@psu.edu
[b]Electronic mail: bjg@psu.edu
[c]Electronic mail: lz2n@virginia.edu

the *ablation* regime, when the fluence exceeds the so-called ablation threshold, collective processes such as explosive boiling and hydrodynamic motion occur in the surface region and the thermal desorption model is no longer valid. The composition of the ejected plume changes dramatically at the ablation threshold. A massive material disintegration and removal characteristic of the ablation regime results in the ejection of molecular clusters, which constitute a significant part of the plume. Although the breathing sphere model provided a wealth of information on the parameters of the ejected plume, it is computationally limited in both size of the simulated system (up to a hundred of nanometers) and time (up to a nanosecond) and it cannot address the further development of the expanding plume.

As soon as the local Knudsen number in the ablated plume becomes high enough to provide the rarified conditions, the long-term plume evolution can be modeled using one of the methods of the rarified gas dynamics (RGD). The results of the MD simulations suggest that in the case of short, 15–150 ps, laser pulses and strongly absorbing matrices, the rarified conditions are established by the time of about one nanosecond after the irradiation. Following Bird,[18] the RGD techniques can be roughly divided into two groups: ''mathematical'' and ''physical.'' The mathematical methods are based on the analytical or numerical solution of a given (almost invariably Boltzmann) equation, which itself is derived using physical approximations. The physical methods are based directly on the simulation of the physics of the gas flow and do not depend on a mathematical model. Since the presence of clusters and cluster reactions (e.g., condensation, evaporation) in the ablation plume make even the derivation of the mathematical equations a challenging task, in our computational model we adopt one of the most powerful physical methods: direct simulation Monte Carlo (DSMC).

In this work, we present a combined MD - DSMC model and apply it to the analysis the evolution of the plume ejected in the ablation regime. The results of a large-scale MD simulation obtained by the end of 1 ns are used as an input for a DSMC simulation of the following plume expansion. The next section discusses the DSMC method and a proposed method for the information transfer from the MD breathing sphere model to the DSMC model. The third section describes the results of the application of the combined model to the simulation of the plume expansion into a vacuum.

II. COMPUTATIONAL MODEL

In this section, the implementation of the DSMC method in the proposed hybrid model is outlined (subsection A), a proposed statistical procedure of the information transfer from MD model to the DSMC model is explained in detail (subsection B), a concurrent problem of characterization of the interparticle interaction is discussed (subsection C), and a computational setup pertinent to a chosen set of initial conditions is described (subsection D).

A. General issues associated with the DSMC modeling of the ablation plume expansion

The DSMC method, developed by Bird for rarefied gas dynamics, has become a standard technique for the simulation of wide class of particle interaction processes, including rarefied gas dynamics,[19] plasma,[20] laser-ablated metal plume development,[11] magnet cluster growth.[21] It has been found to be well suited for treating reaction systems with nonequilibrium distributions, coupled gas dynamics and reaction effects, and emission and absorption of radiation.[22]

In order to adopt results of a MD simulation as an input for a DSMC calculation, we have to characterize both the statistical distribution of the MD output (e.g., spatial monomer and cluster distributions, translational and internal energy distributions) and possible reactions between the monomers, clusters and/or the background gas. In the conventional DSMC description, clusters of each size constitute a separate species. In the ablation regime, the range of cluster sizes can extend up to tens of nanometers (tens of thousands of molecules).[15] The presence of clusters makes it difficult to directly apply the DSMC method as the second stage of the suggested hybrid model due to the following obstacles.

(1) A very large number of species (i.e., clusters of each size) and extremely low fraction of large clusters do not permit direct representation of all clusters in a cell.
(2) The cell size, defined by the local mean free path at the end of the MD stage (possibly as small as 20 nm), is comparable to the size of the largest clusters (up to 15 nm). This condition violates the DSMC assumption about point-sized particles.
(3) The standard DSMC procedure of selection of collision pairs may be either ineffective or incorrect if there is a very large mass variation in a cell.[18]

The use of different weight factors, i.e., the numbers of real particles that are represented by each simulation particle, for monomers and clusters could resolve the first obstacle. This approach, however, is not recommended because of problems with the energy and momentum conservation causing random walks.[18] Boyd's scheme[23] permits exact linear momentum conservation in the case of a two-species gas mixture, but the proposed technique for approximate energy conservation may also cause random walks and is not directly applicable for a multispecies mixture. Moreover, an application of this approach to simulations with *tens of thousands* species is computationally prohibited due to unacceptable memory storage requirements and a very long computational time.

An approach that we adopt in this work is to represent a statistical sample of clusters in a cell rather than clusters of each size. The computational requirements and restrictions for the proposed modification of the DSMC are not known. The quantities of interest in DSMC are usually sample statistics calculated and stored on the level of a cell, e.g., flow velocity or translational temperature. The robustness or degree of error of a statistic when the distribution from which the statistic is drawn is unknown is the subject of the so-called Bootstrapping procedure.[24] In this procedure, an estimate of the distribution of the sample statistic is constructed based on the data of the sample being analyzed, usually by repeatedly random resampling from the initial sample, and recalculating the statistic in order to produce a statistical distribution. The requirements for the sample size and for the

resampling number, well known in Bootstrapping, can be used as guidelines for the number of simulation clusters in a cell and the number of runs for the ensemble averaging in the DSMC procedure. The known constraints on the Bootstrapping procedure are a minimum sample size of eight to ten and a minimum number of resamplings for the estimation of statistical moments of 40–50.[25] More rigorous criteria and restrictions are currently under study and the results will be published elsewhere.

Alexander *et al.*[26] have developed a general implementation of the DSMC for dense systems, where the particle size is comparable to that of a cell. This method, however, involves an assessment of the geometric factors with respect to the number density and is not directly applicable to a multispecies problem. In the present work, we overcame the second obstacle by subdividing relatively large cells into small subcells. Collision pairs in this case are chosen from the same subcell.[18]

The third obstacle is overcome by the introduction of a special technique for choosing collision pairs.[18] Species are divided into collisional groups and each pair of collisional groups is assigned its own maximum product of the cross-section and the relative speed, thus eliminating the selection problem at the cost of slightly increased overall computational time.

B. The MD model and statistical estimation of its results

In this section we briefly review the basic features of the breathing sphere model developed for MD simulation of laser ablation of organic solids and discuss the means of statistical characterization of its results. Complete details of the breathing sphere model are given in Ref. 17. The model assumes that each molecule (or appropriate group of atoms) can be represented by a single particle. The parameters of interparticle interaction are chosen to reproduce the properties of an organic material, in this case a molecular solid. In order to simulate molecular excitation by photon absorption and vibrational relaxation of the excited molecules, an additional internal degree of freedom is attributed to each molecule. This internal degree of freedom, or breathing mode, is realized by allowing the particles to change their sizes. The parameters of a potential function ascribed to the internal motion can be used to change the characteristic frequency of the breathing mode and to affect the coupling between internal and translational molecular motions. In effect one can control the rate of the conversion of internal energy of the molecules excited by the laser to the translational and internal motion of the other molecules.

The laser irradiation is simulated by vibrational excitation of molecules that are randomly chosen during the laser pulse duration within the penetration depth appropriate for a given wavelength. Vibrational excitation is modeled by depositing a quantum of energy equal to the photon energy into the kinetic energy of internal motion of a given molecule.

Since in this model each molecule is represented by a single particle and explicit atomic vibrations are not followed, the system size and the time-step in the numerical integration of the equations of motion can be large enough to reproduce the collective dynamics leading to laser ablation and damage on the time of up to few nanoseconds.

The system chosen to model the laser ablation is a molecular solid or matrix used in matrix-assisted laser desorption ionization (MALDI) mass spectrometry experiments. The parameters of the intermolecular potential are chosen to represent the van der Waals interaction in a molecular solid with the cohesive energy of 0.6 eV, elastic bulk modulus of $\sim$5 GPa, and density of 1.2 g/cm^3. A mass of 100 Dalton is attributed to each molecule. For the simulation performed in this work a computational cell of dimensions $40\times10\times90$ nm (253 808 molecules) is used. Periodic boundary conditions in the directions parallel to the surface are imposed. These conditions simulate the situation in which the laser spot diameter is large compared to the penetration depth so that the effects of the edges of the laser beam are neglected.

As was mentioned in the previous subsection, the results of the MD simulation of laser ablation are to provide the initial conditions for the DSMC simulation of the plume expansion. The proposed scheme of the information transfer involves analytical description of the spatial monomer and cluster distributions as well as the translational and internal energy distributions on the basis of the MD results, and subsequent sampling from these distributions to fill the cells with simulation particles in the DSMC model. For the proper sampling we have to make sure that the distributions are mutually independent; otherwise, we must characterize such dependences. Since the MD breathing sphere model implements periodic boundary conditions in the direction parallel to the surface, we reduce the spatial dependence of the statistical distributions to the dependence on height above the surface. To facilitate the estimations in the region of underpopulated clusters (in a typical output of the breathing sphere calculations there are only about one hundred of clusters larger than pentamers), we propose to divide clusters larger than pentamers into two groups. The first group contains clusters of six to nine molecules and the second group contains clusters of 10 molecules and larger. Note that the estimation stage could be omitted and the simulation particles could be directly sampled from the MD output if clusters of each size were well represented in the MD output. Below we outline the estimation procedure for a typical run of the breathing sphere model. The simulation conditions, which are typical for the ablation stress confinement regime,[16] are a laser fluence of 61 J/m^2, a penetration depth of 50 nm and a pulse duration of 15 ps.

1. Velocity distributions

Our previous analysis[15,16,27] has shown that for each cluster size and location, the velocity distribution can be described in terms of the Maxwell distribution with the axial flow velocity component being linearly proportional to the height (z) above the surface

$$f(v_x,v_y,v_z)\propto\exp\left[-\frac{m(v_z-\alpha_m z)^2+m(v_x^2+v_y^2)}{2k_BT(z)}\right], \quad (1)$$

where f is the distribution function, $T(z)$ is the local translational temperature, m is the mass of the particle, v_x, v_y, and v_z are velocity components, α_m is a constant, and k_B is the

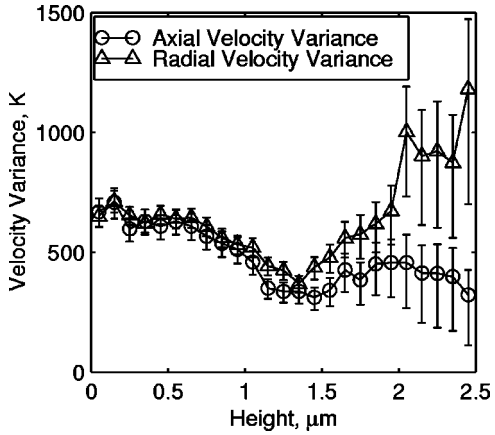

FIG. 1. Axial and radial velocity variances of monomers measured in temperature units at the end of the breathing sphere model calculation (1 ns after the laser pulse). Error bars correspond to 90% confidence interval.

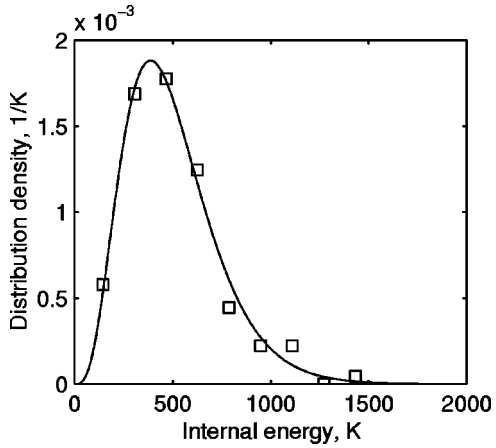

FIG. 2. Distribution of the internal energy of tetramers at the end of the breathing sphere model calculation. The squares represent the MD data, the solid line represents analytic fit to Eq. (3).

Boltzmann constant. It is important to stress that the slopes α_m of the corresponding linear regression lines are equal within the possible statistical uncertainty for all clusters and monomers.[15] Precise examination shows, however, that the spreads in the radial and axial local velocity components are not always statistically equal within the entire plume.

Figure 1 shows the spatial dependence of the variance of radial and axial velocity components of monomers along with 90% confidence limits. It follows from the figure that only the lower half of the monomer flow can be characterized by Eq. (1). The velocity distribution of monomers in the upper part of the flow can be approximated by the elliptical distribution instead.[10] Most of the clusters spatially overlap the lower part of the monomers,[15] and the cluster translational temperatures do not differ significantly from that of the monomers at the same height. Thus, the velocity distributions for clusters are completely characterized by the height above the surface and translational temperature of monomers at that height, while the velocity distribution of monomers is defined by the height above the surface and generally two-component velocity variance, implying the so-called elliptical Boltzmann distribution[10]

$$f(v_x,v_y,v_z)\propto\exp\left\{-\frac{m[v_z-u(z)]^2}{2k_BT_z(z)}-\frac{m[v_x^2+v_y^2]}{2k_BT_{xy}(z)}\right\}, \tag{2}$$

where T_z and T_{xy} are the so-called perpendicular and parallel ''temperatures,'' and u is a flow velocity.

2. Internal energy distributions

No significant dependence of the internal energy on z for each cluster size is noteworthy.[15] Since the statistical uncertainty in estimation of the translational temperature of clusters is on the order of 100%, we cannot conclude whether the translational and internal temperatures are statistically independent. By virtue of our hypothesis about translational equilibrium for these clusters at a given height, however, and because of the strong dependence of translational temperature of monomers of z while the internal energy is independent on z, we may assume such independence. The physical reason for this independence is that at a time of 1 ns the clusters do not reach overall equilibrium, most probably because of a small number of inelastic collisions per cluster.[9]

Significant scatter in the internal energy of clusters of a given size[15] implies statistical characterization of the internal energy. It is well known[28] that the internal energy E_{int} of a molecule/cluster with ν internal degrees of freedom has a Gamma distribution at equilibrium:

$$f(E_{\text{int}})=\frac{1}{\Gamma\left(\frac{\nu}{2}\right)\cdot k_BT_{\text{int}}}\left(\frac{E_{\text{int}}}{k_BT_{\text{int}}}\right)^{\nu/2-1}\exp\left(-\frac{E_{\text{int}}}{k_BT_{\text{int}}}\right), \tag{3}$$

where Γ is the Gamma function and T_{int} is the internal temperature of the clusters. The internal energy of a cluster in MD was estimated from the kinetic energy of translational molecular motion in the center of mass frame of reference,[15] assuming that a cluster of size N has 3 rotational, $3N-6$ kinetic vibrational and $3N-6$ potential vibrational degrees of freedom (dimers have two rotational, one kinetic vibrational, and one potential vibrational degrees of freedom) and using the equipartition theorem. Therefore, for the MD estimations, $\nu=3N-3$, while in the following sampling for the DSMC calculations, $\nu=4$ for dimers and $\nu=6N-9$ for larger clusters. The MD data show good agreement with the theoretical prediction [Eq. (3)]. As an example, Fig. 2 depicts the distribution of internal energy of tetramers calculated as described earlier on the basis of MD results. Note, that the parameter T_{int} in Eq. (3) depends on the cluster size.[15]

3. Cluster size distributions

If a cluster belongs to either of the two cluster groups, the random cluster size must be statistically characterized in addition to the estimations described above. For the first group (clusters of six to nine molecules) we used the power-law distribution[15]

$$f(N)\propto N^{-\delta}, \tag{4}$$

where δ is the power-law exponent. No significant correlation between cluster size and its location is noteworthy for this group. Larger clusters, however, exhibit strong correla-

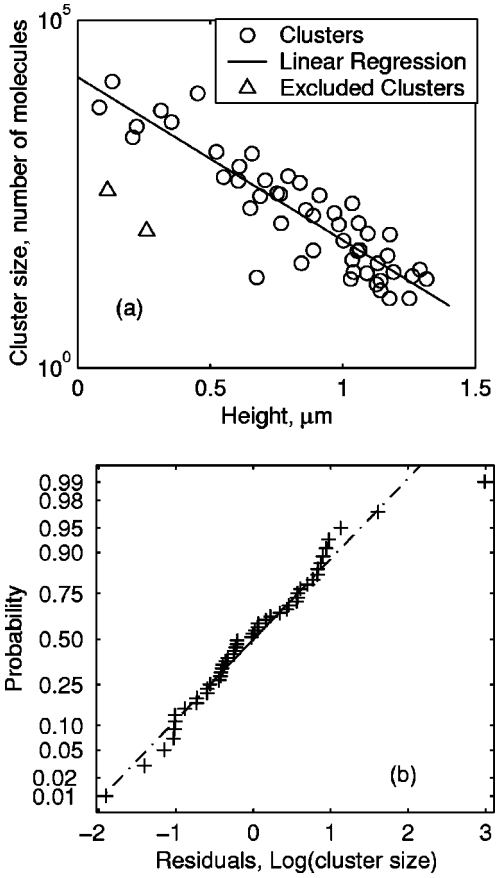

FIG. 3. Spatial distribution of clusters larger than decamers at the end of the breathing sphere model calculation (a) and a corresponding normal plot of the residuals of the linear regression model (b).

tion between their size and height above the surface.[15,29] This correlation may be reduced to a linear regression model.

Figure 3(a) shows the relation between the height above the surface and the cluster size for clusters larger than decamers in semilogarithmic scale. The two clusters shown by triangles are most likely outliners, i.e., they do not belong to the main population.[30] The corresponding linear regression line is built on the basis of the remaining clusters, which are shown by circles. Figure 3(b) shows a normal probability plot of the residuals. It is seen that a fairly large portion of the data are close to the straight line, leading to the conclusion that the normal distribution is a reasonable approximation for the residuals. Therefore,

$$f[\log(N)|z] \propto \frac{1}{\sigma}\exp\left\{-\frac{[\log(N)-\mu\cdot z+b]^2}{2\sigma^2}\right\}, \quad N \geqslant 10, \tag{5}$$

where μ and b are the estimated slope and intercept of the linear regression line, respectively, and σ is the estimated standard deviation of the residuals, implying a conditional lognormal distribution of the cluster size for a given height above the surface. The unconditional, i.e., the overall size distribution for large clusters can be derived by integration of the conditional one by the height-dependent spatial number density of large clusters and following normalization.

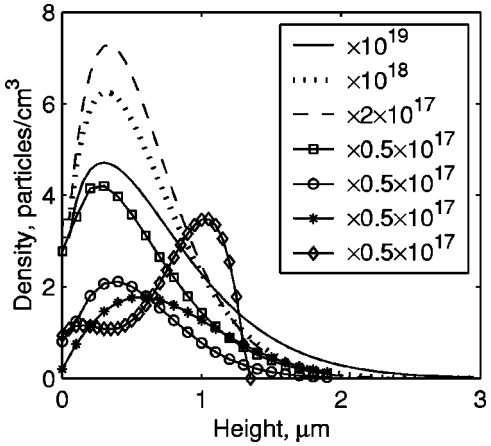

FIG. 4. Estimated number densities of particles in the plume at the end of the breathing sphere model calculation. The solid line represents monomers, the dotted line represents dimers, the dashed line represents trimers, the squares represent tetramers, the circles represent pentamers, the stars represent clusters of six to nine molecules, and the diamonds represent clusters of ten molecules and larger.

The lognormal distribution model has been successfully applied for fitting data on cluster size in both experiments[31–33] and Monte Carlo simulations[34] of the cluster aggregation process. The experimental and simulation conditions were spatially uniform. Theoretically, the lognormal distribution emerges as the asymptotic solution to the Smoluchowski equation of cluster growth under spatially uniform conditions.[35] Recalling that in the MD output, all clusters at each height above the surface have the same translational temperature and axial flow velocity, we may regard the corresponding conditions for cluster reactions as being uniform for a given height. On the other hand, the process of initial cluster formation in the stress-confined regime can be related to a ductile spallation.[16] Baker *et al.*[36] have shown that the latter process results in a piecewise lognormal distribution, i.e., the mass distributions, for example, of, large and small ejected fragments are both lognormal but with different parameters. In the MD simulations we find that the clusters of different masses are located at different heights above the surface [Fig. 3(a)]. Thus, the suggested conditional lognormal distribution of cluster size at a given height [Eq. (5)] can result from cluster reaction processes and/or from the initial spallation.

To fill a cell in DSMC with simulation clusters larger than pentamers, the number of simulation clusters of each cluster group in the cell is calculated as a product of the corresponding number density, the cell volume, and the weight factor. The cluster size is the assigned in accordance with the cluster size distribution within the group [Eq. (4) or (5)].

The spatial number densities were estimated separately for monomers, dimers, trimers, tetramers, pentamers, and the two cluster groups. Figure 4 visualizes the estimated number densities as functions of the height above the surface.

C. Modeling of particle interactions and calculation of the reaction cross sections

1. Particle interactions

Besides the initial and boundary conditions, a variety of possible cluster interactions should be addressed in the DSMC procedure. In general, the interactions may include but not limited to the following reactions:[37]

(1) Simple elastic collision or simple exchange collision (i.e., with possible exchange of molecules between the colliding clusters). Simple collisions and simple exchange collisions are indistinguishable from the Monte Carlo point of view.

$$A_i + A_j \rightarrow A^*_{i+j} \rightarrow A_i + A_j ;$$

(2) Stripping or rearrangement collision ($i+j=k+l$)

$$A_i + A_j \rightarrow A^*_{i+j} \rightarrow A_k + A_l ;$$

(3) Fragmentation collision ($i+j=k+l+m+\ldots$)

$$A_i + A_j \rightarrow A^*_{i+j} \rightarrow A_k + A_l + A_m + \ldots ;$$

(4) Sticking collision

$$A_i + A_j \rightarrow A^*_{i+j};$$

(5) Thermal decomposition or evaporation of a small (monomer, dimer, etc.) cluster

$$A_i \rightarrow A_{i-j} + A_j .$$

Note that sticking as formation of the collision complex A^*_{i+j} inevitably presents in all types of collisions.

Venkatesh *et al.*[38] have shown that the rates of cluster reactions are sensitive to the type of interatomic potential used in the simulation as well as to the parameterization of the potential. This implies that we cannot directly employ the data available in literature for a variety of interatomic potentials[37–43] to our system, where the intermolecular interaction is described by a modified Morse potential.[17] However, the *common tendencies* listed below can be implemented for the modeling of cluster reactions.

(1) For all cluster reactions, their cross sections can be approximated by hard sphere geometric cross sections. The approximation quality is better for larger cluster sizes.
(2) The lifetime of a collision complex A^*_{i+j} has an exponential distribution with the rate described by the Rice–Ramsperger–Kassel (RRK) theory.[44]
(3) The main channels for monomer–cluster reactions are simple or simple exchange collisions and sticking, the former channel diminishes at a cluster size above 8–10.
(4) A large enough cluster cannot be broken in a collision; i.e., there exists a critical cluster size i^* such that if at least one of the colliding clusters has the size equal or larger than i^*, the collision can only be either simple elastic or sticking.[45]
(5) The larger the cluster size, the likelier its collision with another cluster or monomer is a sticking collision.

Our breathing sphere model MD simulation study of cluster collisions is currently in progress, and the following assumptions on the cluster reactions adopted in the DSMC model are based on the literature results summarized earlier and on our initial MD results. We assume that cluster–cluster collisions are elastic ones if both colliding clusters are composed of less than ten molecules and are sticking collisions otherwise. By ''sticking collision'' we mean a collision whose collision complex does not disintegrate within the DSMC time step. Cluster–monomer collisions are elastic collisions if the cluster is smaller than decamer, and are sticking collisions otherwise. A collision complex has the same physical properties as clusters. A monomer can evaporate from a cluster with the rate of monomer evaporation described by RRK theory. A collision between a particle and the surface of the ablated target is always a sticking collision.

Since the contribution of small clusters to the total yield is low in the output of the MD model (clusters of two to nine molecules in size constitute about 8.5% of the overall mass of the plume[46]), we believe that our relatively rough approximations will not affect significantly the distributions of monomers, large clusters, and the overall plume density.

2. Calculation of the reaction rates

Since we model elastic or sticking interactions between particles as hard sphere collisions, the equivalent hard sphere cross sections must be assessed. For monomers, the equivalent cross section can be evaluated from the interaction potential.[18] To this end, the dependence of the impact parameter (b) on the deflection angle (χ) is numerically calculated for various velocities and fitted to such dependence of the hard sphere collision

$$b(\chi) = 2 r_1 \cos(\chi/2), \tag{6}$$

where r_1 is the equivalent hard sphere diameter. The average equivalent radius is 3.45 Å, while the deviation range in the considered relative velocity range (100–400 m/s) is within 5%.

For clusters, the hard sphere equivalent radii r_{hs} are calculated based on the cluster radius of gyration r_{gyr}[34,37]

$$r_{hs} = \sqrt{\tfrac{5}{2}} r_{\mathrm{gyr}} + r_1 . \tag{7}$$

For dimers through pentamers we use the tabulated radii of gyration to calculate the equivalent hard sphere radii. For larger clusters we use interpolation between the radii of gyration of a pentamer and the bulk material (density of 1.2 g/cm^3 and molecular mass of 100 Dalton[17]) to evaluate the equivalent radius[34] of a cluster of N molecules

$$r_{hs}(N) = 2(N^{1/3} \cdot 3.208 + 0.779) + r_1 , \quad [\text{Å}]. \tag{8}$$

The rate of monomer evaporation from a cluster of N molecules with internal energy E_N is calculated according to the classical RRK theory[44]

$$\gamma_N = \nu_0 g_N \left[\frac{E_N - D(N)}{E_N} \right]^{\nu_N}, \tag{9}$$

where $\nu_0 = 10^{12}$ s^{-1} is the typical molecular vibrational frequency,[16] ν_N is the number of available vibrational degrees of freedom, $\nu_N = 1$ for dimers and $\nu_N = 3N-6$ for larger clusters, g_N is the number of surface molecules and $D(N)$ is the molecular evaporation energy. For small clus-

ters, we define the number of surface molecules for the most stable configuration, and for large clusters we use the following approximation:[47]

$$g_N=(36\pi)^{1/3}(N^{1/3}-1)^2. \tag{10}$$

For dimers through pentamers we compute the unimolecular evaporation energy $D(N)$ by subtracting the binding energy of the daughter cluster from that of the mother one at zero temperature, whereas for larger clusters we calculate $D(N)$ by the following formula:

$$D(N)=0.6-0.73[N^{2/3}-(N-1)^{2/3}], \quad [\mathrm{eV}], \tag{11}$$

which interpolates between the values for a pentamer and bulk material. The corresponding elastic energy release (E_k) shared between the monomer and the daughter cluster is modeled by the Engelking theory, which has been found to be suitable for relatively low internal energies.[48] In this theory, the distribution function of the kinetic energy release E_k is given by

$$P(E;E_k)=(\nu-2)(\nu-3)E_k\frac{(E-E_k-D)^{\nu-4}}{(E-D)^{\nu-2}}, \tag{12}$$

where E, ν, and D are the internal energy, the number of degrees of freedom and the evaporation energy of the mother cluster, respectively.

D. Computational setup

In this study, we choose a simple case of a flat spatial laser profile with a fluence of 61 J/m^2, penetration depth 50 nm, and a pulse duration of 15 ps, which makes it possible to use the results of a single MD simulation[16] performed for a surface area of 40×10 nm^2 as a uniform input for the DSMC simulation of the plume ejected from the whole laser spot with a radius of 10 μm.[46]

The advantage of the axial symmetry of a problem, which has often been taken in DSMC simulations of laser desorption,[10,11] is that it allows us to reduce the number of independent geometric coordinates to just two (radius and height). The corresponding reduction in cell number results in a significant saving of the computational time and memory. Note that the particle motion remains fully three-dimensional. In our DSMC simulations the cylindrical volume surrounding the plume above the laser-ablated surface is divided in both radial and axial directions into annular cells and filled with simulation particles. The estimated number density of monomers to pentamers is sufficiently high to represent these types of particles in each cell, therefore, the simulation particles in each cell represent monomers, dimers, trimers, tetramers, pentamers, and the proposed randomly sampled clusters from each of the two groups of larger clusters (see Sec. II B). We use the novel no-time-counter variant of the DSMC, which has several advantages over the traditional time counter DSMC method.[18]

The weight factor W, i.e., the number of real particles represented by a simulation particle, is assessed on the basis of the requirements to the minimum representation of particles in a cell (Sec. II A). We adopt a minimum number of eight random-sized simulation clusters in a cell for clusters from each group and a minimum number of 50 runs of the code for the ensemble averaging. The corresponding weight factor W also guarantees the required minimum representation of monomers to pentamers. To fill a cell with simulation particles, the number of simulation particles of each species in the cell is calculated as a product of the corresponding number density, the cell volume, and the weight factor. Then, for each species that belongs to one of the two cluster groups, the particle mass is assigned in accordance with the cluster size distribution within the group. The velocity and internal energy for each particle are sampled from the corresponding estimated distributions, and the particle position is chosen at random within the cell. For monomers and well-represented clusters (dimers through pentamers) the procedure is the same except for the random mass. Other specific details of the simulation setup are outlined below.

The initial cell size is 50 nm in the axial direction and 250 nm in the radial direction; each cell is divided into 16 subcells to fulfill the constraints on the mean free path and the particle size (see Sec. II A). To increase the efficiency of the algorithm, the cell structure is changed two times during the simulation. The total number of particles is 4.5 million and the weight factor is 4 000. To address the selection problem (see Sec. II A), the particles are divided into the following four *sampling* groups (not to confuse with the two cluster groups): (i) monomers to decamers, (ii) clusters of 11 to 100 molecules in size, (iii) clusters of 101 to 1000 molecules in size and (iv) clusters large than 1000 molecules in size. The maximum product of cross section and relative velocity is assigned to each pair of groups and is updated during the calculations. Our simulations stopped at a time of 500 ns, when the collision frequency approaches zero. The results obtained are discussed in the next section.

III. RESULTS AND DISCUSSION

In this section we present the results of the DSMC simulation of the ablation plume expansion for the initial conditions provided by a large-scale MD simulation as described earlier. The results on the time evolution of the ablation plume in terms of the density profiles and velocity distributions for both monomers and large clusters (subsections A and B), distribution of internal energy of large clusters (subsection C), and integral plume characteristics (subsection D) are presented and discussed.

A. Time evolution of the plume

The time evolution of the density of monomers is visualized in Fig. 5. It is observed that the initially cylindrical gas cloud changes its shape and becomes more elliptical with time. A splitting of the spatial distribution of the monomers is visible in the distributions plotted for times of 100 and 300 ns. This effect is attributed to the time delay between sticking and evaporation reactions among large clusters and monomers.[46] For times of 100 and 300 ns, the shapes of molecular clouds are geometrically similar. The density profiles become similar when each flow velocity component becomes self-similar; i.e., a linear dependence on the corresponding coordinate is established. While for the axial component such dependence has been developed by the end

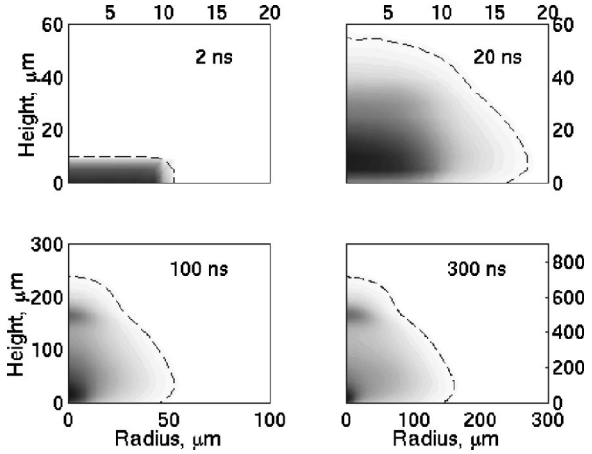

FIG. 5. Time evolution of spatial number density of monomers. The dotted contour lines correspond to 2% of the maximum density. The aspect ratio is the same in all plots.

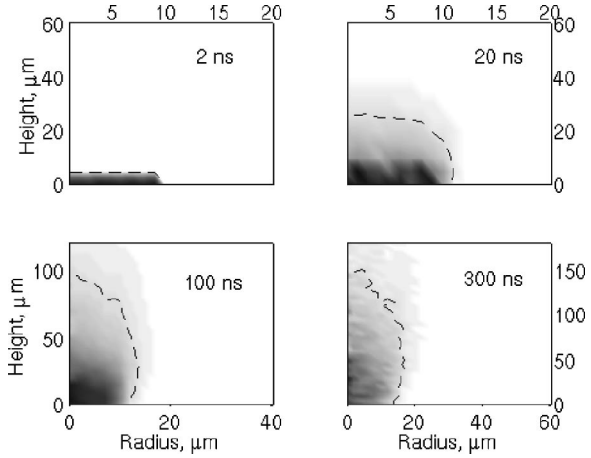

FIG. 7. Time evolution of plume density. The dotted contour lines correspond to 5% of the maximum density. The aspect ratio is the same in all plots.

of the MD simulations, during the first nanosecond of the ablation process, the formation of a self-similar flow in the radial direction requires much longer time. We can estimate this time[6] by dividing the radius of the laser spot (10 μm) by the average speed of sound (about 250 m/s), which gives 40 ns.

The development of a radial flow for monomers is shown in Fig. 6. At time 2 ns, the maximum flow velocity (920 m/s) is slightly lower than four times the average speed of sound, as predicted by Kelly for unsteady adiabatic expansion.[6] At time 20 ns a further increase of the radial front speed is visible. This increase can be attributed to monomer evaporation from large and relatively hot clusters, in accordance with the dynamic source model of Chen *et al.*[8] The self-similar flow establishes at the estimated time (about 40 ns), while a few minor convexities of the curve can be attributed to the monomer evaporation from large clusters (see below).

The time evolution of the overall plume density (Fig. 7) is somewhat different from that of monomers. Although density plots at times 100 and 300 ns appear to be similar in shape, they are not geometrically similar. The image extension along the axial coordinate is larger than that along the radial coordinate, which results in a sharpening of the density pattern. This phenomenon has been observed experimentally in laser ablation of large analyte molecules embedded into a matrix of small molecules in MALDI.[49] Since large clusters make a major contribution to the total yield (clusters larger than decamers constitute more than 65% of the plume mass[46]), they are responsible for the characteristic density shapes (see, Fig. 7).

While the pressure gradient governs the formation of the self-similar expansion of the monomers, the main driving force for the flow formation in the case of large clusters is collisions with monomers and light clusters.[49] The time needed for formation of a self-similar flow of large clusters can be, therefore, much greater than the 40 ns required for the monomers. Figure 8 visualizes the evolution of radial flow velocity of large clusters. The maximum flow velocity increases from 40 m/s at 2 ns up to 260 m/s at 300 ns. The pronounced concavity, which causes nonsimilar density pattern (see Fig. 7) is clearly visible for times up to 300 ns.

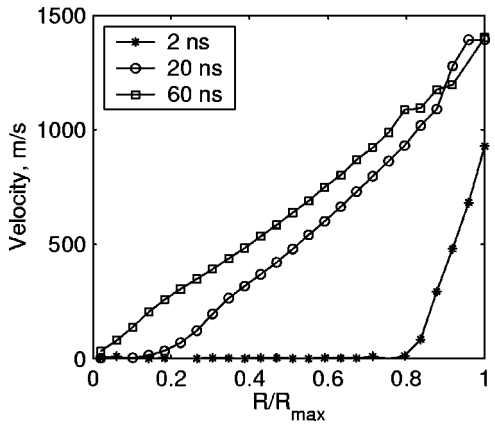

FIG. 6. Time development of radial flow of monomers. The horizontal axis is a radial distance R from the plume axis, divided by the maximum lateral extension R_{max} of monomers at the corresponding time.

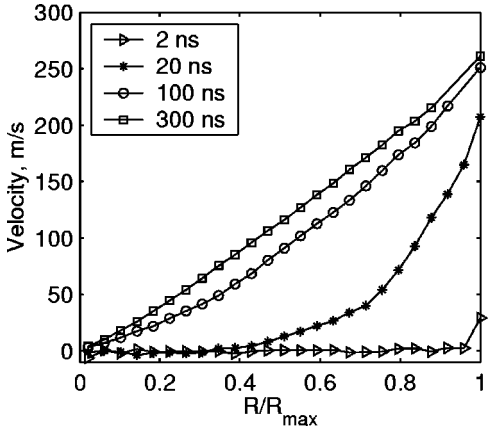

FIG. 8. Time development of radial flow of clusters larger than 50 molecules in size. The horizontal axis is a radial distance R from the plume axis, divided by the maximum lateral extension R_{max} of these clusters at the corresponding time.

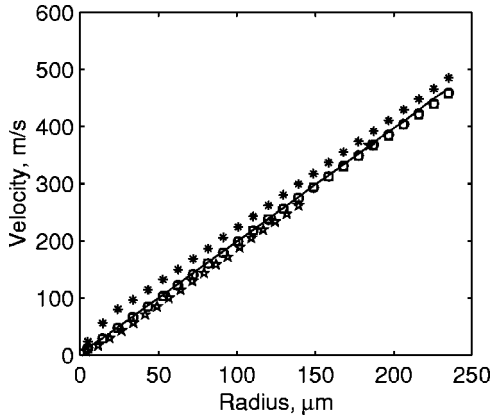

FIG. 9. Flow of different particles in the lateral direction at 500 ns. The pentagrams represent clusters of 11 molecules and larger, the squares represent clusters of three to nine molecules, the circles represent dimers, the stars represent monomers, and the straight line represents monomers located higher than the main population of large clusters.

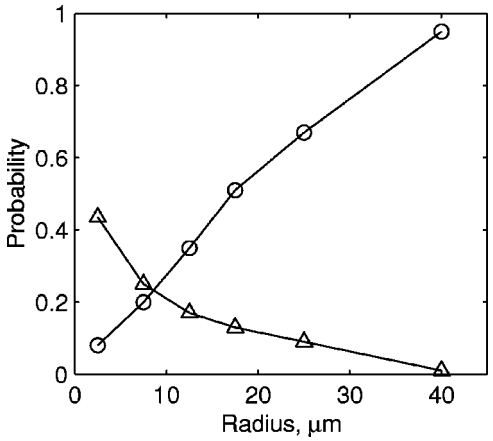

FIG. 10. The calculated probability of a free flight throughout the plume of an evaporated monomer versus the location of the mother cluster. The curves are shown for the inward (triangles) and outward (circles) velocity directions of the evaporated monomer at time 100 ns. For monomers evaporated in the inward direction, only distance traveled to the axis is taken into account; the increase of the estimated mean free path due to the following plume expansion is disregarded. The axial locations of the mother clusters are at heights 20–60 μm.

In multispecies self-similar expansion, the different species develop a similar flow velocity[6,50] if the number of collisions between the particles is sufficiently high, or the distance traveled by particles in a free flight stage of expansion is high relative to the range of interparticle distances at the previous, collisional expansion stage. The self-similar flow, formed in the axial direction at the MD stage is characterized by the same flow velocities of different particles at the same height,[15] which can be attributed to the collective character of the ablation process driven by the relaxation of the laser-induced pressure[16] as well as a large number of the collisions within the initial dense vapor cloud. Figure 9 shows the flow of different particles in the lateral direction at 500 ns. For dimers, light clusters, and large clusters, the flow dependences on the radius are very close to the same linear dependence, which can be attributed to high distances traveled by particles in a free flight, since the collision probability becomes low at a time of about 100 ns. The overall flow velocity of monomers is somewhat higher. This observation can be attributed to the contribution of the monomers, which are continuously evaporating from large hot clusters.

Let us illustrate this thesis by the following example. If the local mean free path for a monomer is λ and an evaporated monomer has traveled a small distance dL during which λ is approximately constant, then the probability P_{dL} that the monomer has not collided while traveling is given by

$$P_{dL} = \exp\left(- \frac{dL}{\lambda} \right). \tag{13}$$

The probability P_L of a monomer having a free flight while traveling an arbitrary distance L is then given by

$$P_L = \exp\left[- \int_L \frac{dL}{\lambda(L)} \right]. \tag{14}$$

Figure 10 shows the calculated probability of a free flight throughout the plume of an evaporated monomer versus the location of the mother cluster. The curves are shown for the inward and outward velocity directions of the evaporated monomer at 100 ns; for monomers evaporated in the inward direction only the distance traveled to the axis is accounted for, the increase of the estimated mean free path due to the following plume expansion is disregarded. The axial locations of the mother clusters were considered at heights 20–60 μm where the monomer density is high at this time (see Fig. 5).

It is clearly seen from Fig. 10 that the monomers evaporated in the outward direction have much larger probability to fly freely across the plume. Since the plume aspect ratio is high (see Fig. 7), the probability of a free flight of a monomer evaporated in the direction parallel to the axis is close to zero. Therefore, the outward direction is ''preferable'' for the evaporated monomers, which results in a higher lateral flow velocity of monomers (see Fig. 9). Indeed, the radial flow velocity calculated for only those monomers that are located higher than the main population of large clusters (straight line on Fig. 9) coincides with the flow velocities of other particles.

B. Velocity distribution

The simulation methods used (MD and DSMC) allow for the analysis of the empirical distributions of physical characteristics of the particles. The distribution of monomer velocity is of the most interest because it can be compared to the velocity distribution in the desorption regime, which was found to comply with the elliptical Boltzmann distribution[10] [Eq. (2)]. Moreover, monomers participate in all kinds of the interactions considered. We visualize the velocity distribution with the aid of the variance of each velocity component (axial, radial, and tangential) measured in temperature units. The distributions are shown for the following two regions: (i) region close to the plume axis [axial profile, Fig. 11(a)] and (ii) region close to the bottom of the plume [radial profile, Fig. 11(b)]. Each region consists of a layer of cells second to the axis origin in the corresponding direction. Both profiles indicate that at large times the velocity distribution cannot be

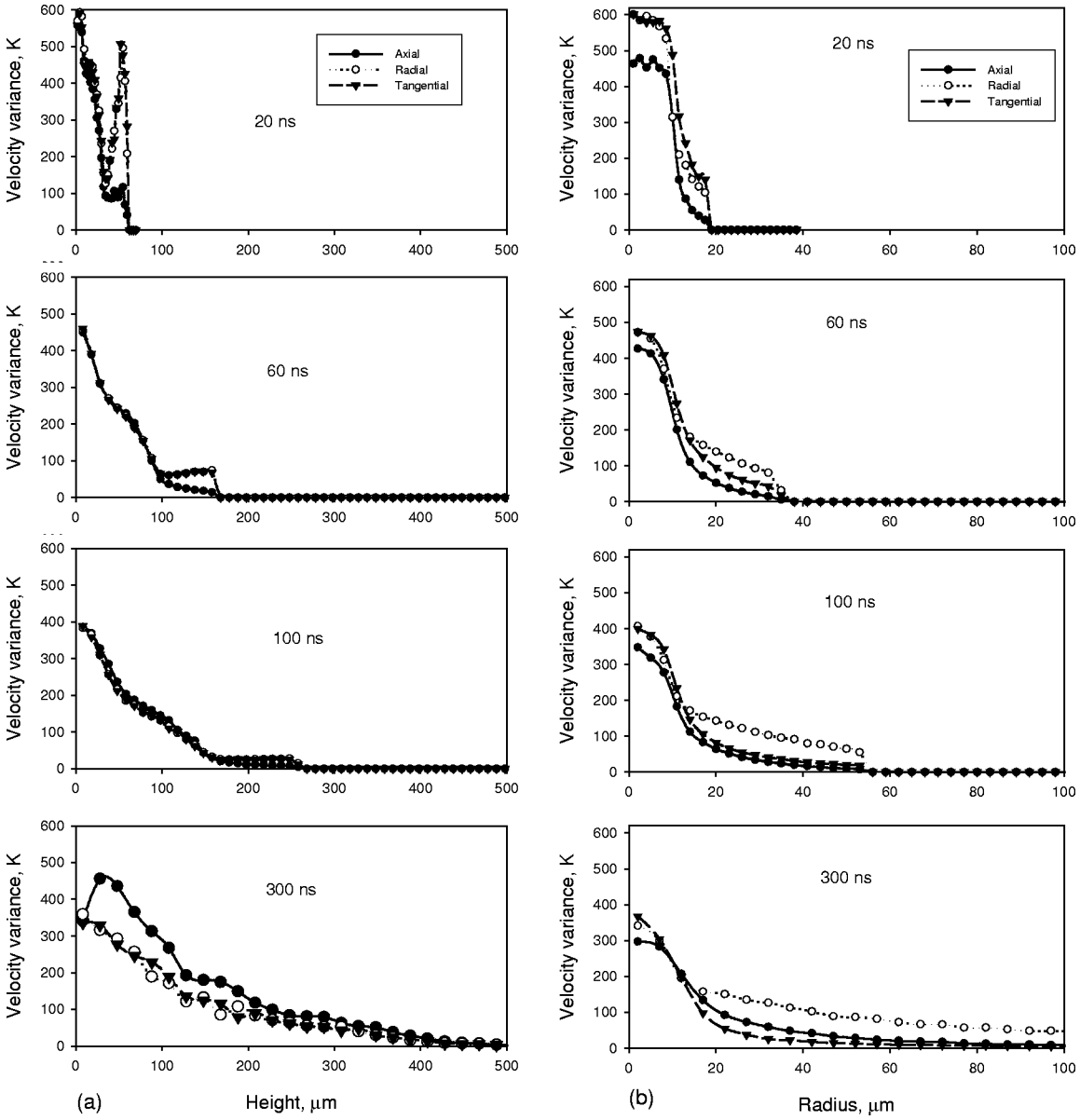

FIG. 11. Profiles of the statistical variances of monomer velocity components, calculated at regions (a) close to the plume axis and (b) near the irradiated surface. The 90% confidence error bars are smaller than the size of the symbols.

characterized by a simple model like, e.g., the elliptical distribution with spatially independent temperatures.

Since the expansion in the axial direction is self-similar from the ever beginning of the DSMC simulation, no thermal nonequilibrium is seen in the lower part of the plume up to a time of 100 ns [see Fig. 11(a)]. In Figs. 11(a) and 11(b), we plot the velocity variances only for cells in which the monomer density is larger than one percent of the maximum monomer density. Since in the course of self-similar expansion the upper part of the plume expands faster, this low-density region of strong thermal nonequilibrium, which corresponds to the initial nonequilibrium at the MD stage (see Fig. 1) is not shown on the axial profiles for times 100 and 300 ns. The process of mixing of particles originated at the bottom of the plume (low axial flow velocity but relatively high statistical variance, about 300 K in temperature units) and particles originated at the middle of the plume (large flow velocity but small variance) leads to increase of the measured scatter, mainly in the axial direction, [see Fig. 11(a)]. Therefore, for large times (e.g., 300 ns) the ''perpendicular temperature'' (the axial velocity component variance) on the axial profile exceeds the ''parallel temperature'' (the radial or tangential velocity component variance), while at earlier time the perpendicular temperature is below the parallel temperature. This observation is in agreement with Kelly's comment on a temperature split,[6] which had been predicted by various researchers such that the perpendicular temperature was both higher and lower than the parallel temperature. The physical reason of this tendency is that no normal, i.e., Boltzmann distribution, exists for either velocity component at these times.

In the lateral profiles, [see Fig. 11(b)], the nonequilibrium starts to develop due to the unsteady expansion leading to the formation of a self-similar flow in the lateral direction

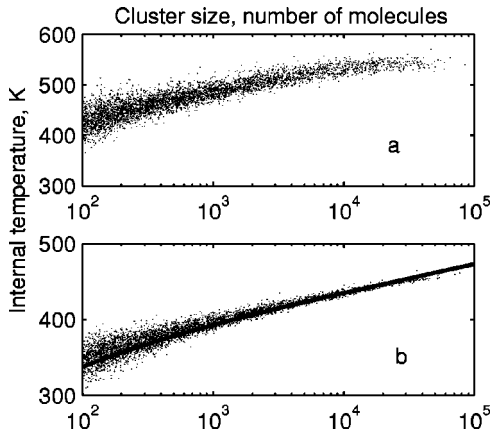

FIG. 12. The internal energy of large (more than 100 molecules in size) clusters at (a) 100 ns and (b) 500 ns. Also shown is the dependence predicted by Eq. (23) for time 500 ns (solid line).

(see Fig. 6). An interesting behavior of the radial profiles is noteworthy. Most existing theories deal with the expansion of the plume in the axial direction, in such a case the splitting of the overall velocity variance into the two components — axial and lateral — is justified. As we see on the axial profiles, this is indeed the case: radial and tangential variances are statistically equal, so we can speak about single parallel ''temperature.'' In the case of the expansion in the lateral direction, the splitting of the overall variance into axial and lateral is no longer justified. The flow direction (radial) should be singled out to give splitting into radial and nonradial (axial and tangential) components, as we see in Fig. 11(b) at 100 ns and later. Moreover, at 300 ns, the axial and lateral profiles are symmetric in the sense that in the axial profile the flow-related axial temperature is higher than its lateral counterpart, and in the radial profile the flow-related radial temperature is higher than its nonradial counterpart. The physical reason for this is that the mixing processes in the flow directions lead to growth of the statistical scatter when the collision rate becomes low. The resultant velocity distribution, measured experimentally [for example, by time-of-flight (TOF) experiments], depends on the interplay between the mentioned processes and may vary with the experimental conditions.

C. Internal energy distribution

Figure 12 visualizes the time evolution of the internal energy of large clusters. In our model, clusters can cool down by evaporation of monomers. For clusters larger than 50 molecules in size, the internal temperature decrease due to one evaporation event can be approximated by[47]

$$\Delta T_N \propto \frac{D(N)}{N}, \tag{15}$$

while the evaporation rate [Eqs. (9) and (10)] is

$$\gamma_N \propto N^{2/3} \exp\left[-\frac{D(N)}{k_B T(N)}\right]. \tag{16}$$

It follows from Eqs. (15) and (16) that smaller clusters with relatively high temperature will cool faster than the larger clusters with lower temperature. However, the dependence of the internal temperature on the cluster size does not become steeper with time. Rather, the temperature dependence tends to keep its pattern during the further slow cooling.

To explain such conservation of the slope of the dependences shown in Fig. 12 let us consider the balance-type equation

$$\frac{\partial p(N)}{\partial t} = p(N+1)\,\gamma_{N+1} - p(N)\,\gamma_N + \psi_N, \tag{17}$$

where $p(N)$ is the probability function of the cluster size, and ψ_N is the rate of cluster growth due to the sticking collisions. In this equation we assume that the evaporation rate is given by Eq. (16) and disregard the statistical fluctuations of the internal temperature for a given cluster size. For times exceeding 100 ns the collision rate becomes low and the latter term in Eq. (17) can be neglected. Also, the cluster size distribution does not evolve in time (the empirical distribution functions of cluster size are statistically equal for time larger than 100 ns). Therefore, for large time we have the following approximate balance equation:

$$p(N+1)\,\gamma_{N+1} = p(N)\,\gamma_N. \tag{18}$$

Taking the two-term Taylor expansion and simplifying for large N, we derive from Eq. (18) the following differential equation:

$$-\frac{d\left[\dfrac{D(N)}{T(N)}\right]}{dN} = k_B \log[\beta(N)], \tag{19}$$

where

$$\beta(N) = \frac{p(N)N^{2/3}}{p(N+1)(N+1)^{2/3}}. \tag{20}$$

The solution of Eq. (19) is then given by

$$T(N) = \frac{D(N)}{k_B\{C - \int_{N_{\min}}^{N} \log[\beta(N)]dN\}}. \tag{21}$$

Figure 12(b) shows the internal temperature of large clusters at time 500 ns along with the predicted curve [Eq. (21)]. The value of parameter C, estimated by the curve fitting ($\hat{C}=17$), is large relative to the value of the integral (the maximum value of the integral in the size range considered is 2.55), therefore, the dependence of the internal temperature on the cluster size is mainly defined by the size dependence of the unimolecular dissociation energy [Eq. (11)].

D. Angular distributions

Angular distributions of the ejected molecules and clusters are important integral characteristics of the plume. Figures 13(a) and 13(b) illustrate the evolution of angular distribution of monomers and angular kinetic energy distribution of the entire plume. These distributions are built under the assumption that the characteristic dimension in an experiment in which the distributions could be measured (e.g., in TOF experiments), is large as compared to the plume size.

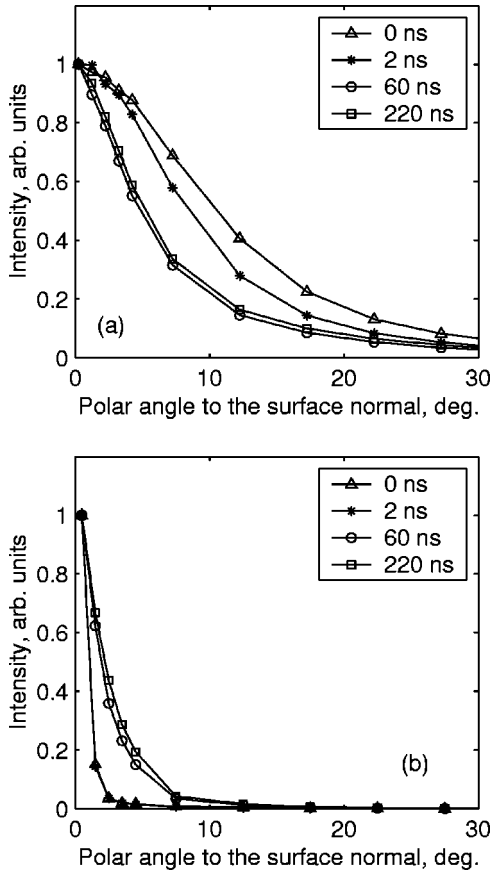

FIG. 13. Time evolution of (a) the angular distribution of monomers and (b) the angular distribution of the kinetic energy in the plume. The later is defined as a relative kinetic energy of particles arriving to a distant detector within an angle interval $[\phi;\phi+d\phi]$.

The forward peaking of the monomer angular distribution is noticeable, while the angular distribution of the kinetic energy exhibits unfocusing to some extent. Kelly proposed[28] that the monomer angular distribution could be described by $\cos^p$ distribution with p related to the Mach number M in the axial flow

$$p \approx (1+M)^2. \tag{22}$$

Equation (22) is based on the assumption that the Boltzmann distribution with a constant axial flow velocity is established, at least for the major part of the plume. As it was shown in the previous subsections, this is not the case in the simulations. Moreover, the angular distributions plotted on Fig. 13 cannot be satisfactorily fitted to a single cosine distribution. Rather, the actual angular distribution can be fitted to a mixture of two cosine distributions. Such fitting was recently implemented in the analysis of experimental data by Elam and Levy.[51]

One possible scenario of the further forward peaking of monomer angular distribution and backward peaking of the angular kinetic energy distribution is the transfer of radial kinetic energy from monomers and light clusters to large clusters. Since the axial flow had developed on the earlier stage described by the MD breathing spheres model, the sticking collisions between monomers and large clusters will not change the axial velocity of clusters on average. They will, however, increase the radial velocity of clusters (see also Sec. III A), resulting in widening of the angular distribution of kinetic energy. The probability of a collision between a monomer and a large cluster is proportional to the relative velocity. Therefore, the monomers with a high radial velocity component are more likely to transfer their kinetic energy to large clusters, leading to the decrease of the average radial velocity of monomers and causing forward peaking of the monomer angular distribution. The evolution of both angular distributions ends by 60 ns, when the rate of collisions becomes low.

IV. CONCLUSIONS

We have presented a simulation study of expansion of a plume into a vacuum in the course of laser ablation of molecular solid. Our two-stage computational model consists of the molecular dynamics breathing sphere model of the initial plume formation followed by the direct simulation Monte Carlo model of the following plume expansion. The procedure requires statistical characterization of the results of the MD model to be implemented by the DSMC model. Analytical descriptions are proposed and verified for the statistical distributions of translational and internal energy of monomers and clusters and for the distribution of the cluster sizes. Although many plume features pertinent to the ablation regime, such as massive ejection of clusters and rapid formation of a self-similar flow in the axial direction, have been revealed by the results of the breathing sphere model, the large-scale simulation study presented here provides new results.

The presence of clusters, directly ejected in laser ablation, drastically changes the evolution of the plume as compared to laser desorption. Besides the direct contribution to the overall plume mass and energy, clusters affect the time evolution of monomers. The appearance of a high-velocity tail in the distribution of a radial velocity component, the forward peaking of the angular distribution, the specific density and velocity patterns are examples of the cluster-induced characteristics of monomers. On the other hand, monomers accelerate clusters in the radial direction causing widening of the angular distribution of the plume kinetic energy. The results pertinent to the considered particular initial conditions are outlined below.

While the plume expansion becomes self-similar in the axial direction at the initial formation stage, i.e., about 1 ns after laser energy deposition, the self-similarity in the lateral direction develops significantly later, from about 40 ns for monomer expansion to 500 ns for large-cluster expansion. This time delay in the formation of the self-similar flow is the main reason for the sharpening effect, observed experimentally.

The velocity distribution of monomers at time 300 ns and larger cannot be fitted to Boltzmann distribution of any kind; rather, it is characterized by a spatially and direction dependent statistical scatter about the flow velocity. It is found that in the plume region close to the axis, the two out of three components (radial and tangential) of the overall velocity variance are statistically equal, which is consistent

with the well-known concepts of ''perpendicular temperature'' and ''parallel temperature.'' However, in the region close to the ablated surface but far enough from the axis, the flow-related component (radial) significantly differs from the other two statistically equal components (axial and tangential). Therefore, the proper split of the ''temperature'' may involve the variance of the velocity component in the flow direction and the variance of either of the other two components perpendicular to the flow.

The shape of the dependence of the internal temperature on the cluster size is established by 100 ns and does not change at a later time, when the collision rate becomes low. It was shown that this dependence is mainly defined by the size dependence of the unimolecular dissociation energy of a cluster.

The pronounced effect of the spatial segregation of clusters in both axial and lateral directions may have direct implementation in the pulsed laser deposition, in which clusters and other surface debris negatively influence the quality of the deposited films.

Some of the quantitative predictions of these first simulations require further verification. More accurate assessment of cluster reactions and their cross sections is an example of what should be addressed in the future work. Finally, the developed methodology of combining MD and DSMC can be implemented in the simulation of nucleation and growth processes. The proposed hybrid MD-DSMC model can be implemented for modeling of condensation processes.

ACKNOWLEDGMENTS

This work was supported through the Medical Free Electron Laser Program by the United States Office of Naval Research and by the Air Force Office of Scientific Research. The computational support was provided by IBM through the Selected University Research Program, and by the Center for Academic Computing at Penn State University.

[1] K. L. Saenger, Processing of Advanced Materials, **3**, 1 (1993).
[2] A. V. Singh, R. M. Mehra, N. Buthrath, A. Wakahara, and A. Yoshida, J. Appl. Phys. **90**, 5661 (2001).
[3] A. Rohrbacher and R. E. Continetti, Rev. Sci. Instrum. **72**, 3386 (2001).
[4] F. Hillenkamp and M. Karas, Int. J. Mass. Spectrom. **200**, 71 (2000).
[5] R. Kelly, Phys. Rev. A **46**, 860 (1992).
[6] R. Kelly, J. Chem. Phys. **92**, 5047 (1990).
[7] A. V. Gusarov, A. G. Gnedovets, and I. Smurov, J. Appl. Phys. **88**, 4352 (2000).
[8] K. R. Chen, T. C. King, J. H. Hes, J. N. Leboeuf, D. B. Geohegan, R. F. Wood, A. A. Puretzky, and J. M. Donato, Phys. Rev. B **60**, 8373 (1999).
[9] I. NoorBatcha, R. R. Lucchese, and Y. Zeiri, J. Chem. Phys. **86**, 5816 (1987).
[10] D. Sibold and H. M. Urbassek, J. Appl. Phys. **73**, 8544 (1993).
[11] T. E. Itina, W. Marine, and M. Autric, J. Appl. Phys. **82**, 3536 (1997).
[12] H. M. Urbassek and D. Sibold, Phys. Rev. Lett. **70**, 1886 (1993).
[13] M. Handschuh, S. Nettesheim, and R. Zenobi, Appl. Surf. Sci. **137**, 125 (1999).
[14] K. H. Song and X. Xu, Appl. Surf. Sci. **127–129**, 111 (1998).
[15] L. V. Zhigilei, Appl. Phys. A (in press).
[16] L. V. Zhigilei and B. J. Garrison, J. Appl. Phys. **88**, 1281 (2000).
[17] L. V. Zhigilei, P. B. S. Kodali, and B. J. Garrison, J. Phys. Chem. B **101**, 2028 (1997); *ibid*., **102**, 2845 (1998).
[18] G. A. Bird, *Molecular Gas Dynamics and the Direct Simulation of Gas Flows* (Clarendon, Oxford, 1994).
[19] J. Struckmeier and K. Steiner, Phys. Fluids **7**, 2876 (1995).
[20] S. Dietrich and I. D. Boyd, J. Comput. Phys. **126**, 328 (1996).
[21] H. Mizuseki, Y. Jin, Y. Kawazoe, and L. T. Wille, J. Appl. Phys. **87**, 6561 (2000).
[22] S. Dunn and J. B. Anderson, J. Chem. Phys. **99**, 6607 (1993).
[23] I. D. Boyd, J. Thermophys. Heat Transfer **10**, 579 (1996).
[24] M. D. Burke and E. Gombay, Stat. Probabil. Lett. **12**, 421 (1991).
[25] B. Efron, J. Am. Stat. Assoc. **85**, 79 (1990).
[26] F. J. Alexander, A. L. Garcia, and B. J. Adler, Phys. Rev. Lett. **26**, 5212 (1995).
[27] L. V. Zhigilei and B. J. Garrison, Appl. Phys. Lett. **71**, 551 (1997).
[28] R. Kelly and R. W. Dreyfus, Nucl. Instrum. Methods Phys. Res. B **32**, 341 (1988).
[29] L. V. Zhigilei, Mater. Res. Soc. Symp. Proc. **677**, AA2.1.1 (2001).
[30] V. Barnett and T. Lewis, *Outliers in Statistical Data* (Wiley, New York, 1994).
[31] F. Frank, W. Schulze, B. Tesche, J. Urban, and B. Winter, Surf. Sci. **156**, 90 (1985).
[32] J. G. Pruett, H. Windischmann, M. L. Nicholas, and P. S. Lampard, J. Appl. Phys. **64**, 2271 (1988).
[33] J. Chaiken, M. J. Casey, and M. Villarica, J. Phys. Chem. **96**, 3183 (1992).
[34] B. Briehl and H. M. Urbassek, J. Vac. Sci. Technol. A **17**, 256 (1999).
[35] M. Valerica, M. J. Casey, J. Goodisman, and J. Chaiken, J. Chem. Phys. **98**, 4610 (1993).
[36] L. Baker, A. J. Giancola, and F. Allahdadi, J. Appl. Phys. **72**, 2724 (1992).
[37] R. Venkatesh, R. R. Lucchese, W. H. Marlow, and J. Schulte, J. Chem. Phys. **102**, 7683 (1995).
[38] R. Venkatesh, W. H. Marlow, R. R. Lucchese, and J. Schulte, J. Chem. Phys. **104**, 9016 (1996).
[39] R. D. Kay, L. M. Raff, and D. L. Thompson, J. Chem. Phys. **93**, 6607 (1990).
[40] H. Balamane, T. Halicioglu, and W. A. Tiller, Phys. Rev. B **46**, 2250 (1992).
[41] D. G. Vlachos, L. D. Schmidt, and R. Aris, J. Chem. Phys. **96**, 6880 (1992).
[42] J. Jellinek and Z. B. Guvenc, Z. Phys. D: At., Mol. Clusters **19**, 371 (1991).
[43] J. W. Brady, J. D. Doll, and D. L. Thompson, J. Chem. Phys. **71**, 2467 (1979); **73**, 2767 (1980); **74**, 1026 (1981).
[44] M. F. Jarrold, in *Clusters of Atoms and Molecules*, edited by H. Haberland (Springer, Berlin, 1994), p. 163.
[45] H. Hettema and J. S. McFeaters, J. Chem. Phys. **105**, 2816 (1996).
[46] M. I. Zeifman, B. J. Garrison, and L. V. Zhigilei, Appl. Surf. Sci. (in press).
[47] A. V. Malakhovskii and M. Ben-Zion, Chem. Phys. **264**, 135 (2001).
[48] S. Weerasinghe and F. G. Amar, J. Chem. Phys. **98**, 4967 (1993).
[49] A. A. Puretzky, D. B. Geohegan, G. B. Hurst, M. V. Buchanan, and B. S. Luk'yanchuk, Phys. Rev. Lett. **83**, 444 (1999).
[50] L. V. Zhigilei and B. J. Garrison, Rapid Commun. Mass Spectrom. **12**, 1273 (1998).
[51] J. W. Elam and D. H. Levy, J. Phys. Chem. B **102**, 8113 (1998).